



HAL
open science

High-temperature absorption cross-sections and interference-immune sensing method for formaldehyde near $3.6 \mu\text{m}$

Nicholas Kuenning, Isabelle Sanders, Nicolas Q Minesi, Daniel Pineda, R. Mitchell Spearrin

► To cite this version:

Nicholas Kuenning, Isabelle Sanders, Nicolas Q Minesi, Daniel Pineda, R. Mitchell Spearrin. High-temperature absorption cross-sections and interference-immune sensing method for formaldehyde near $3.6 \mu\text{m}$. *Journal of Quantitative Spectroscopy and Radiative Transfer*, 2023, pp.108690. 10.1016/j.jqsrt.2023.108690 . hal-04121619

HAL Id: hal-04121619

<https://hal.science/hal-04121619v1>

Submitted on 8 Jun 2023

HAL is a multi-disciplinary open access archive for the deposit and dissemination of scientific research documents, whether they are published or not. The documents may come from teaching and research institutions in France or abroad, or from public or private research centers.

L'archive ouverte pluridisciplinaire **HAL**, est destinée au dépôt et à la diffusion de documents scientifiques de niveau recherche, publiés ou non, émanant des établissements d'enseignement et de recherche français ou étrangers, des laboratoires publics ou privés.



Distributed under a Creative Commons Attribution 4.0 International License

High-temperature absorption cross-sections and interference-immune sensing method for formaldehyde near 3.6 μm

Nicholas M. Kuenning^{a,*}, Isabelle C. Sanders^a, Nicolas Q. Minesi^a, Daniel I. Pineda^b, R. Mitchell Spearrin^a

^a*Department of Mechanical and Aerospace Engineering, University of California, Los Angeles (UCLA), Los Angeles, CA 90095, USA*

^b*Department of Mechanical Engineering, The University of Texas at San Antonio (UTSA), San Antonio, TX, 78249, USA*

Abstract

Absorption cross-sections of formaldehyde (CH_2O) were measured at elevated temperatures near 3.6 μm , a region of strong intensity due to the overlapping $^{\text{Q}}\text{Q}_5$ branch of the ν_1 band and the $^{\text{P}}\text{Q}_7$ branch of the $\nu_2+\nu_4$ combination band. 1,3,5-trioxane was shock-heated in an argon bath gas to produce controlled mixtures of formaldehyde over a range of temperatures (900–1500 K) and pressures (0.4–4.8 atm). Spectrally-resolved absorption measurements of formaldehyde were obtained using a rapidly-tunable distributed-feedback interband cascade laser scanned at 40 kHz over 2778.1–2778.9 cm^{-1} behind reflected shock waves. The resulting absorption cross-sections were fit with functions reflecting the temperature and pressure dependence of the targeted features, enabling spectral reconstruction at any temperature and pressure within the range of the study. By exploiting the strong temperature and pressure sensitivity of the cross-sections, it is demonstrated that CH_2O concentration, temperature, and pressure can be inferred from a measured absorbance spectrum. Cross-sections of common combustion species were also measured over the selected wavelength range to validate that the region is largely free of narrow-band interference. Further, the multi-parameter spectral fitting method is shown to correct for baseline interference and demonstrated in experiments involving transient gas properties.

Keywords: cross-sections, absorption spectroscopy, formaldehyde, H_2CO , CH_2O , high-temperature

1. Introduction

Formaldehyde (CH_2O , H_2CO , HCHO), or methanal, is an important molecule in biology, medicine, polymer chemistry, atmospheric chemistry, combustion chemistry, and astronomy. Spectroscopy of CH_2O is relevant for remote sensing of protostellar environments [1] and cometary tails [2]. Most pertinent to the current work, CH_2O is an intermediate species in all hydrocarbon combustion, and is particularly prominent in the oxidation regimes of next-generation low-emission heat engines [3]. Thus, in-situ spectroscopic measurements of CH_2O are important to the study of combustion systems and other high-temperature environments [4]. Spectroscopic reference data at high-temperature conditions are needed to enable such measurements.

CH_2O is a prolate asymmetric top molecule with C_{2v} molecular symmetry [5] and six vibrational modes which render a rich and complex infrared spectrum. A myriad of fundamental, overtone, and combination vibrational bands comprise the dense infrared spectrum yielding several regions of strong absorption. Of particular interest for sensing applications has been the overlap of the C–H symmetric and asymmetric stretch bands in the domain of 3.4–3.6 μm , and the C–O stretch band near 5.7 μm .

Several researchers have probed select wavelengths in the infrared absorption spectrum of CH_2O for quantitative in-situ measurement of species concentration at elevated temperatures [6–10]. The spectral regions relevant to these prior works are labeled in Fig. 1. A common challenge in these works is locating regions of strong CH_2O absorption which have minimal interference from other species common to combustion, namely CH_4 near 3.6 μm and H_2O near 5.7 μm . Observing Fig. 1, the region near 3.6 μm was selected for this study due to very strong CH_2O absorption at elevated temperatures, while remaining largely free of common combustion interferers. Figure 2 offers a closer comparison of the the magnitude of CH_2O absorbance relative to common interferers within the targeted spectral region of this study. As shown, this domain involves overlapping Q-branches from the ν_1 (C–H symmetric stretch) band and the $\nu_2+\nu_4$ (C–O stretch + H–C–H out-of-plane vibration) combination band.

The number of infrared active vibrational modes of CH_2O inherently leads to a very large number of possible transitions, or lines, which can be difficult to fully account for in line-by-line modeling. This challenge is exacerbated at elevated temperatures when more high rotational energy states are populated and more lines meaningfully contribute to observed spectra. The population of high rotational states at elevated temperature also increase the likelihood of band overlap, as observed in the domain

*Corresponding author

Email address: kuennign@ucla.edu (Nicholas M. Kuenning)

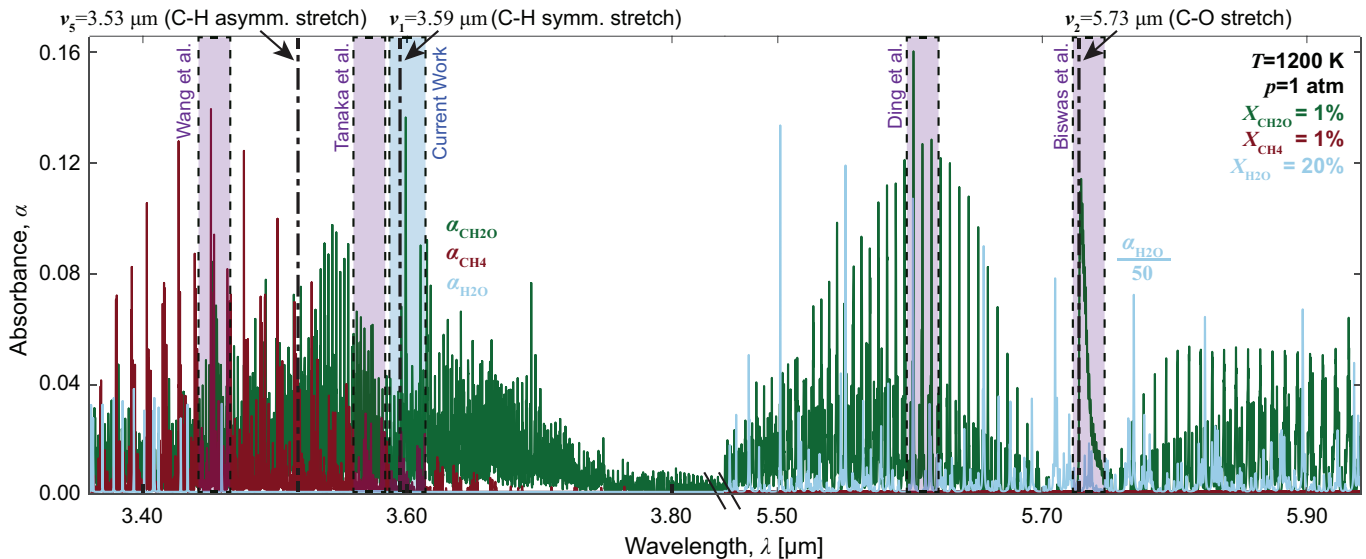


Figure 1: Formaldehyde, methane, and water absorbance plot between 3.4–3.8 μm and 5.5–5.9 μm . The water absorbance between 5.5–5.9 μm has been scaled by a factor of 1/50. The spectral region studied in this work is highlighted in blue while the regions studied in similar works are highlighted in purple.

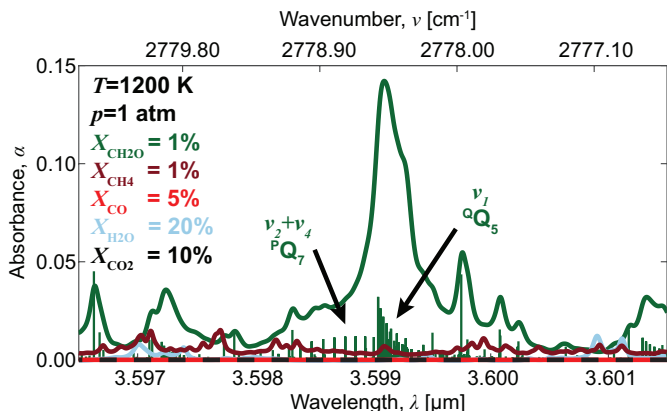


Figure 2: Absorbance plot of formaldehyde and potential interferers within the spectral region relevant to this study. A stick plot of the formaldehyde absorption bands is shown underneath the absorbance feature.

near 3.6 μm . These factors, along with collisional effects at elevated pressures, blend spectral transitions and complicate modeling. Prior experimental and computational spectroscopy studies have been performed to help build formaldehyde line lists in databases such as HITRAN and GEISA [11, 12]. Unfortunately, the HITRAN and GEISA formaldehyde line lists are limited to relatively low-lying rotational states populated at room temperature. The AITY line list (accessible through ExoMol) provides a spectroscopic database for CH_2O accounting for higher energy states [13–15]. The line list includes many more transitions and has improved agreement with data at elevated temperatures, as can be seen in Fig. 3. Despite such improvement, residual disagreements with measured

cross-sections near 3.6 μm remain significant, highlighting the need for more experimental data to serve both as reference spectra for inferring molecular abundance and as validation targets for further database and modeling improvement.

This paper describes two contributions related to formaldehyde spectroscopy: (1) a unique high-temperature dataset of CH_2O absorption cross-sections near 3.6 μm , and (2) a novel interference-immune sensing method for inferring CH_2O molecular abundance, temperature, and pressure simultaneously using tunable laser absorption spectroscopy in combustion environments. Experimental methods including the shock-heating apparatus (i.e. shock tube), gas mixture preparation, and the rapid spectral-scanning optical setup are described. Resulting measurements of CH_2O cross-sections in an argon bath gas in the spectral domain of 2778.1–2778.9 cm^{-1} at temperatures of 900–1500 K and pressures of 0.4–4.8 atm are presented. Measured cross-sections are fit using a linear regression, providing coefficients to reconstruct the cross-section at any temperature, pressure, and wavenumber within the range of the study. Using the established cross-section database, a method is developed to infer temperature, pressure, and CH_2O mole fraction from the local spectral structure without prior knowledge of baseline intensity, broadband absorption, path length, or mole fraction. Additional analysis is performed to quantify the effect of common combustion interferers and how such interference is mitigated. The multi-parameter sensing method is demonstrated via measurements during chemical kinetics experiments involving CH_2O formation. In aggregate, this work provides a basis for robust and quantitative measurements of CH_2O in dynamic, high-temperature environments and contributes to the body of experimental reference data on formaldehyde

spectroscopy.

2. Theory

2.1. Absorption Spectroscopy

Here we briefly describe the basic elements of spectroscopic theory used in this work to define terms and notation. Spectral absorbance, $\alpha(\nu)$, associated with the target species is calculated using the ratio of transmitted light (I_t) to incident light (I_0) as defined by the Beer-Lambert law:

$$\alpha(\nu) = -\ln\left(\frac{I_t}{I_0}\right)_\nu = X_{\text{abs}}PL \sum_j S_j(T)\phi_j(\nu, T, \Delta\nu_C(T, P, X_Y)) \quad (1)$$

In Eq. 1, ν [cm^{-1}] is the wavenumber, X_{abs} is the mole fraction of the absorbing species, P [atm] is the pressure, L [cm] is the path length, S_j [$\text{cm}^{-2}/\text{atm}$] is the linestrength of transition j , T [K] is the temperature, ϕ_j [cm] is the lineshape function of transition j , and X_Y represents the dependence of the lineshape function on the gas composition due to collisional broadening. The collisional width of the line, $\Delta\nu_C$, is given by Eq. 2 in which $\gamma_{\text{CH}_2\text{O}-Y}$ is the collisional broadening coefficient.

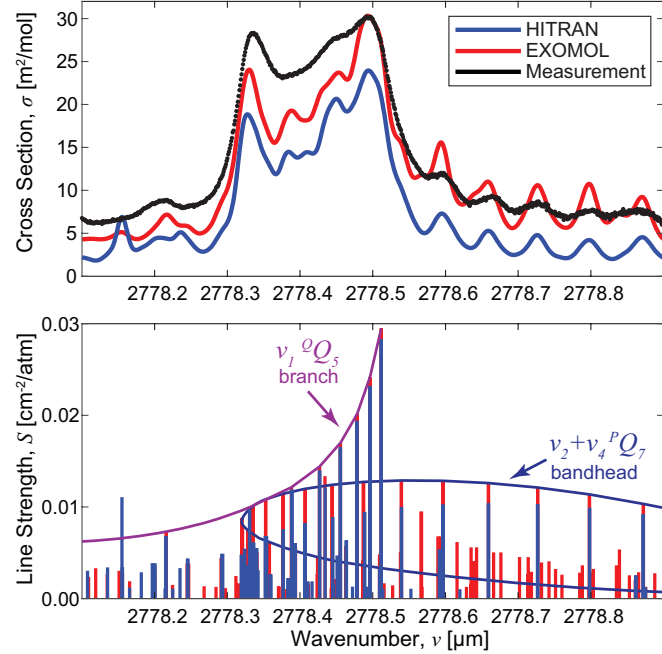


Figure 3: Comparison among absorption cross-section (Top) and line strengths (Bottom) predicted using HITRAN and ExoMol databases. Experimental data at $T = 1120$ K, $p = 0.82$ atm, and 1% CH_2O in He are included in the absorption cross-section plot. Simulations were performed at the same conditions as the experiment. The HITRAN simulation uses line-by-line He broadening coefficients provided in HITRAN and the ExoMol simulation uses the average of the HITRAN broadening coefficients within the simulated spectral range.

$$\Delta\nu_C = P \sum_Y X_Y 2\gamma_{\text{CH}_2\text{O}-Y}(T) \quad (2)$$

Equation 1 is useful when comprehensive line-by-line databases are available for the target species, and we use this form of the Beer-Lambert law in Section 2.2 for performing spectral simulations using the HITRAN and ExoMol databases [11, 15]. However, line-by-line summation is less tractable for larger molecules with a larger number of energy states and associated transitions, for which comprehensive databases are lacking (especially at high temperature conditions). Line-by-line summation is also challenging in spectral domains that are highly convoluted due to line broadening and mixing between many neighboring transitions with overlapping lineshape distributions. The absorption cross-section, σ_{abs} [m^2/mol], represents an aggregate of the linestrength and lineshape function at a given wavenumber, temperature, and pressure. Equation 3 defines the absorption cross-section as a function of S_j and ϕ_j multiplied by the universal gas constant \mathcal{R} [8.314 J/mol·K], T , and a unit conversion factor:

$$\sigma_{\text{abs}}(\nu, P, T, X_Y) = \mathcal{R}T \cdot \frac{1}{1013.25} \sum_j S_j(T)\phi_j(\nu, T, \Delta\nu_C(T, P, X_Y)) \quad (3)$$

The absorption cross-section provides a useful scaling parameter for wavelength-specific molecular absorptivity that can be characterized as a function of temperature and pressures when line-by-line parameters are not easily deconvolved. Equation 4 shows a modified version of the Beer-Lambert Law that is obtained by substituting Eq. 3 into Eq. 1, subverting the line-by-line summation to determine absorbance at a given condition from an absorption cross-section.

$$\alpha(\nu) = X_{\text{abs}}PL\sigma_{\text{abs}}(\nu, P, T)/\mathcal{R}T \cdot 1013.25 \quad (4)$$

2.2. Existing Spectral Databases

The HITRAN and ExoMol databases provide line-by-line spectroscopic parameters associated with many CH_2O transitions near $3.6 \mu\text{m}$ [11, 15], the targeted spectral region in this work. Line-by-line absorbance simulations require parameters that define transition-specific collisional broadening, $\gamma_{\text{CH}_2\text{O}-Y}$, which are partly captured in the aforementioned databases. While the current HITRAN database provides collisional broadening coefficients for each line reported, the ExoMol database contains coefficients only for transitions associated with the lowest rotational quantum numbers [16]. As a first-order comparison, the average of the HITRAN collisional broadening coefficients of CH_2O was employed to simulate the absorbance using the linecenters, linestrengths, and lower state energies from the ExoMol database. Figure 3 compares the

predicted absorption cross-section near $3.6\ \mu\text{m}$ using line-by-line simulations with each database assuming He as the collision partner alongside an experimental measurement of the CH_2O absorption cross-section in a He bath gas.

The top of Fig. 3 shows that absorption simulations using parameters from the HITRAN database predict lower absorption than simulations using parameters from the ExoMol database, while both simulations predict a lower overall absorption cross-section than is observed experimentally. These disagreements can be better explained by examining the underlying transitions. The bottom of Fig. 3 includes a stick plot of the temperature-dependent linestrengths calculated using each database. Within the simulated region, the ExoMol database contains more lines than the HITRAN database and generally predicts higher linestrengths for lines shared between the two databases. These differences lead to better agreement between the ExoMol database and the experimentally measured cross-sections in the region between $\nu = 2778.5$ and $2778.9\ \text{cm}^{-1}$. In this region, the observed disagreement seen in Fig. 3 is likely due to inaccuracies in the assumed broadening coefficients. Between $\nu = 2778.1$ and $2778.5\ \text{cm}^{-1}$, both databases consistently underpredict absorbance suggesting that both databases are either missing high-temperature transitions and/or contain inaccurately low linestrengths in that region. It should be further noted that potential line mixing at the bandhead of the ${}^P Q_7$ branch of the $\nu_2 + \nu_4$ combination band may also be responsible for the local underprediction [17, 18]. Rather than attempt to generate the presumed missing lines or characterize the line mixing and broadening, we measure absorption cross-sections over a range of temperatures and pressure to characterize the absorptivity of this convoluted spectral region.

3. Experimental setup

The absorption spectra of CH_2O near $3.6\ \mu\text{m}$ were obtained using a tunable interband cascade laser scanned over the wavelength domain of $2778.1\text{--}2778.9\ \text{cm}^{-1}$. Measurements at high-temperature were enabled by a shock tube facility, depicted in Fig. 4. Hot CH_2O was formed by shock-heating mixtures containing 1,3,5-trioxane in argon. Absorption cross-section measurements were taken over a range of conditions spanning temperatures from $900\text{--}1500\ \text{K}$ and pressures from $0.4\text{--}4.8\ \text{atm}$. In this section, we detail the experimental configuration, including the high-enthalpy shock tube and optical hardware used in this work, as well as the related preparation, measurement, and analysis procedures.

3.1. Optical setup

High spectral-resolution investigation of the CH_2O absorption features near $3.6\ \mu\text{m}$ was enabled by a continuous-wave distributed feedback (DFB) interband cascade laser (ICL) (Nanosystems and Technologies GmbH), used to access the individual rovibrational transitions comprising the overlapping ${}^Q Q_5$ branch of the ν_1 (C-H symmetric stretching) band and the ${}^P Q_7$ branch of the $\nu_2 + \nu_4$ (C-O stretch + H-C-H out-of-plane vibration) combination band. The ICL can be tuned in wavenumber from 2775 to $2781\ \text{cm}^{-1}$ and has a nominal output power of $8.3\ \text{mW}$ near $2778.5\ \text{cm}^{-1}$. A $40\ \text{kHz}$ triangle waveform of injection current was used to tune the ICL across a $1.03\ \text{cm}^{-1}$ scan depth to resolve the entirety of the targeted spectral features near $3.6\ \mu\text{m}$. The laser scan rate and waveform provided an effective raw measurement rate of $80\ \text{kHz}$ including the up and down scans. This raw spectral measurement rate could be down-sampled or averaged to improve SNR (signal-to-noise ratio). The injection current was modulated below the lasing threshold to mitigate the

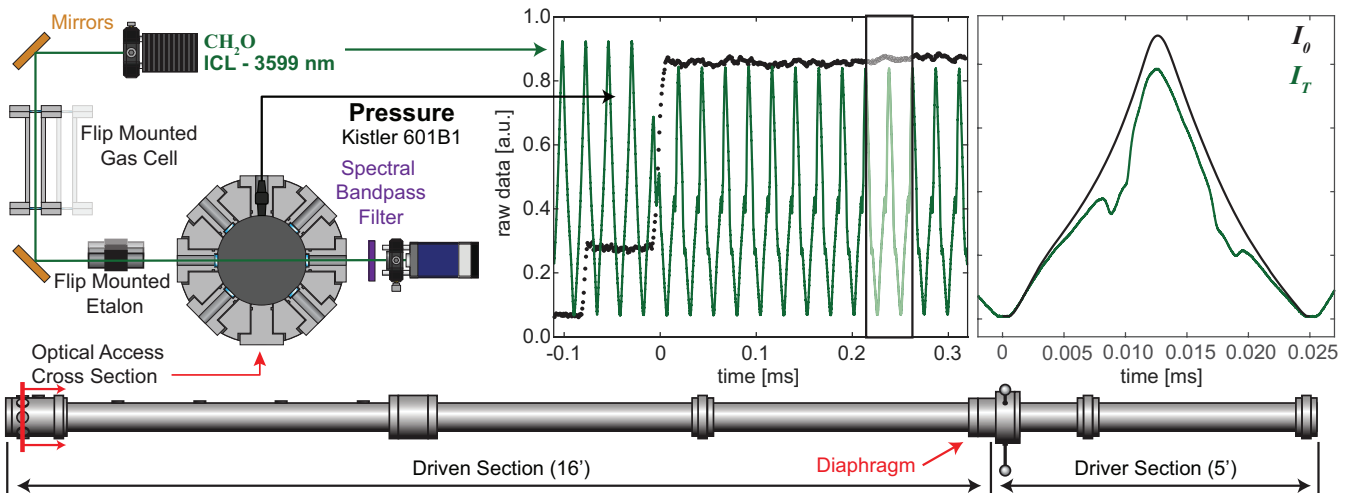


Figure 4: (Top-left) Cross-section of optical access to shock tube with laser, gas cell and detector. (Top-middle) Raw detector and pressure transducer data of the incident and reflected shock regions. (Top-right) Raw detector signal of attenuated light, I_T , plotted on top of the pre-shock background signal, I_0 . (Bottom) Side view of shock tube with optical access location and diaphragm location labeled.

effects of thermal emission from the hot gases in the shock tube.

The optical arrangement of the laser absorption sensor on the high-enthalpy shock tube is shown in Fig. 4. The transmitted laser radiation is passed through an optical iris and a bandpass spectral filter (Andover, 3600 ± 140 nm) to minimize thermal emission before being focused onto a thermo-electrically cooled photovoltaic (PV) detector (VIGO System PVI-4TE-6-1). For each measurement of transmitted intensity I_t , a corresponding background I_0 is recorded in the absence of a mixture to establish a baseline for calculation in Eq. 4. The relative frequency of the laser light is determined by placing a germanium etalon with a free spectral range of 0.0241 cm^{-1} in the path of the beam using an optical flip-mount. Additionally, shocks were run in pure Ar to quantify the effect of beam steering on the transmitted signal. Beam steering effects were generally limited to the first laser scan period which was not used in data analysis.

3.2. Wavenumber calibration

During the experiment, time-resolved absorbance data is captured following the passage of the reflected shock. Additional information is required to convert the time-resolved data into spectrally-resolved data. First, the relative wavenumber of the scan is determined by placing the aforementioned germanium etalon in the beam path and recording the attenuated light. The temporal spacing between peaks of constructive and destructive interference provides a mapping between time and wavenumber in the scan, provided that the free spectral range (FSR) is known. FSR is a function of the length and index of refraction of the etalon, each with its own uncertainty. In this arrangement, the absolute wavenumber is unknown and measurements cannot be reliably calibrated against existing spectral databases for CH_2O due to the significant disagreement between simulations and measurements is noted in Fig. 3. An independent reference is therefore required to confirm the FSR and establish the absolute wavenumber range captured in the scan.

The P branch of the $\nu_2+\nu_4$ combination band of methane contains three strong room temperature transitions within the spectral range of the scan. Two of the transitions are grouped around $\nu = 2778.06$ cm^{-1} and the other is located at $\nu = 2778.64$ cm^{-1} ; notably, all three lines can be accessed without changing the laser temperature or injection current. The HITRAN database lists the uncertainties of these linecenters as <0.01 cm^{-1} . Methane data were recorded before every test to account for day-to-day laser drift; the FSR never deviated more than 0.05% and the linecenter position never deviated more than 0.025 cm^{-1} over the course of the measurement campaign. Methane measurements taken before and after the reflected shock tests produced no noticeable change on the timescale of hours. As such, we estimate a corresponding spectral position uncertainty of <0.01 cm^{-1} .

3.3. Mixture preparation

At room temperature, formaldehyde is not sufficiently stable at substantial enough quantities to be used directly in test mixtures of interest. Thus, we required a molecule to serve as the formaldehyde source. 1,3,5-trioxane readily decomposes into three formaldehyde molecules at elevated temperatures and has a sufficient vapor pressure to be used in test gas preparation. However, due to its relatively low vapor pressure at room temperature and polarity, 1,3,5-trioxane may condense onto or adsorb into the walls of vessels that it occupies. The corresponding change in gas concentration (within a diluted mixture) depends on many factors, including the respective gas system volumes, metal type/surface roughness, and partial pressure of 1,3,5-trioxane [19]. Common methods for handling adsorbing molecules in shock tube experiments are: 1) Passivate the shock tube walls by filling the tube with the adsorbing molecule, promptly vacuum this mixture and then re-fill with a mixture of the desired concentration; 2) heat the shock tube walls to reduce adsorption and raise the vapor pressure; and 3) allow the molecule to partially adsorb and then measure the resulting concentration immediately before the shock [20].

For this study, we used a combination of passivation and direct measurement of trioxane concentration just prior to the shock tube experiment. Due to a lack of an existing database for trioxane absorption in this region, we performed a room-temperature spectroscopic study of trioxane using a small optical gas cell with a longitudinal path length of 26.34 cm. In this trioxane cross-section study, the small diameter gas cell was connected to a gas delivery manifold, itself connected to vacuum pumps and a borosilicate glass flask containing the crystalline 1,3,5-trioxane. The trioxane absorption measurements were performed over the length of the gas cell as opposed to transversely, as in the shock tube configuration. This configuration allowed for an initial fill with pure trioxane followed by back-filling the gas cell with argon to achieve a target concentration percentage without concern for longitudinal variation that could distort the measurement. The integrated absorption from the initial pure trioxane gas sample was used to calibrate the gas mixture concentration. The gas pressure in the cell was monitored using a capacitance manometer (MKS Baratron 627D). Absorption cross-sections were recorded over a range of experimentally relevant pressures (10 to 250 Torr) for a mixture of 0.5% trioxane. This concentration was selected to provide sufficient absorbance in the 10.32 cm path length of the shock tube while also minimizing the amount of trioxane in the mixture to mitigate the temperature drop associated with endothermic dissociation after the shock. The trioxane cross-sections are reported in [Appendix A](#). With well-characterized cross-sections of trioxane at relevant concentrations, the shock tube test mixture composition could be readily determined before each experiment despite some inherent procedural variability.

3.4. Shock tube experiments

A high-enthalpy shock tube was used to generate high temperatures (>800 K) via near-instantaneous shock heating of test gases with diluted 1,3,5-trioxane. The trioxane is shock-heated to produce targeted quantities of formaldehyde, as has been successfully performed by others previously [6, 8–10]. The shock tube facility used is described in prior works by the authors [17, 18, 21], and is shown in Fig. 4. The driven and driver sections of the shock tube are connected to vacuum pumps, an agitated mixing tank, and a gas delivery manifold used to barometrically prepare the mixtures for the experimental measurements. Mixtures of 1,3,5-trioxane and argon are prepared in the agitated mixing tank and allowed to mix for a minimum of 30 minutes. Before filling each mixture into the shock tube, the separate gas cell was filled with methane and data were recorded to determine both the absolute wavenumber range of the experiment and FSR, as described in Section 3.2. For each test, the gas cell was then removed from the beam path and the shock tube was subsequently filled with 1,3,5-trioxane mixture and allowed to passivate over 5 minutes to avoid a substantial change in composition between the trioxane measurement and shock. One minute before each shock, the attenuated laser light from the 1,3,5-trioxane was recorded to later infer the initial (pre-shock) gaseous trioxane concentration from the trioxane cross-section database (Appendix A).

The test section of the shock tube has an internal diameter of 10.32 cm, defining the path length L in Eq. 4. Interchangeable ports holding a dynamic pressure transducer (Kistler 601B1) and optical windows circumscribe the test section 2 cm from the shock tube end wall, as shown in Fig. 4. The pressure transducer records the pressure time history of the incident and reflected shock wave through a charge amplifier (Kistler Type 5018A), and five piezoelectric sensors (Dynasen CA-1135) record the time of arrival of the incident shock wave, from which the incident shock velocity and reflected shock test conditions are determined using normal-shock relations [22]. When accounting for vibrational relaxation, the uncertainties in reflected shock temperature T_5 and pressure P_5 are typically about 1–2% [23]. Accounting for the uncertainty in T_5 and the uncertainty due to the dissociation of 1,3,5-trioxane into CH_2O gives a temperature uncertainty of 3%. Example raw voltage data from the detector and transducer charge amplifier, shown in the top of Fig. 4, were recorded at 10 MHz using a Tektronix MS044 acquisition module, triggered to record by the time-of-arrival sensors.

Spectrally-resolved CH_2O absorption measurements at 40 kHz were performed in the shock tube for a reflected shock temperature (T_5) range of 900–1500 K and a reflected shock pressure (P_5) range of 0.4–4.8 atm using scanned-wavelength techniques. Upon shock heating, 1,3,5-trioxane rapidly dissociates into formaldehyde [6]; the rate at which this occurs limits the accessible thermodynamic conditions for this study. For reflected shocks at 1 atm and

at temperatures below ~ 900 K, the trioxane does not complete dissociation before the end of the achievable test time for this shock tube configuration ($\lesssim 2$ ms). Conversely, at 1 atm and above 1500 K, the formaldehyde completely dissociated before a single full scan was complete, providing insufficient data to produce a reliable cross-section.

3.5. Methyl methacrylate experiments

The cross-sections measured in this work were used to determine the time-resolved concentration of CH_2O during the decomposition of methyl methacrylate (MMA) behind reflected shock waves. These experiments were performed as part of the work by Sanders et al. [24] and are described briefly here for context in the sensing demonstration.

Mixtures of approximately 3% methyl methacrylate diluted in an Ar bath gas were barometrically prepared in an agitated mixing tank with its pressure monitored by a capacitance manometer (MKS Baratron 627D). Liquid MMA was evaporated from the aforementioned glass flask and added to the mixing tank before being agitated with the Ar bath gas for a minimum of 20 minutes. To avoid loss of MMA concentration to the walls of the experiment, the mixing tank and shock tube were filled with pure MMA and MMA diluted in Ar, respectively, before being quickly vacuumed and filled to the desired pressure. The remaining procedure of running shocks and collecting data was identical to the procedure described in Section. 3.4.

4. Results and discussion

4.1. Formaldehyde cross-sections

A total of 33 tests were run at varied temperature and pressure conditions within the targeted range. Sample data across two isobars at 0.9 atm and 2.2 atm, along with an isotherm at 1200 K, are shown in the top half of Fig. 5. Four wavelengths labeled λ_1 – λ_4 were chosen to illustrate the pressure and temperature dependence. These four points consist of the spectra’s left wing at 2778.11 cm^{-1} , left peak at 2778.34 cm^{-1} , middle dip at 2778.41 cm^{-1} and right peak at 2778.51 cm^{-1} . The trends at the chosen wavelengths are displayed in the bottom half of Fig. 5. These specific wavelengths are discussed in the subsequent text to highlight the variation of temperature and pressure dependence within the targeted spectra. It should be noted that the entire spectra (including all these wavelengths) are captured within every scan period, and that the full spectra (not individual wavelengths) are used to infer gas properties.

The left wing of the spectra (λ_1) exhibits minimal dependence on temperature and pressure relative to the overall spectra. Within the spectral region, there is no non-absorbing region to serve as a reference point to which non-ideal effects on the spectra from emission, mechanical vibrations and broadband interferers can be corrected. In lieu of a non-absorbing region, λ_1 serves as a reference that maintains a relatively constant value across a

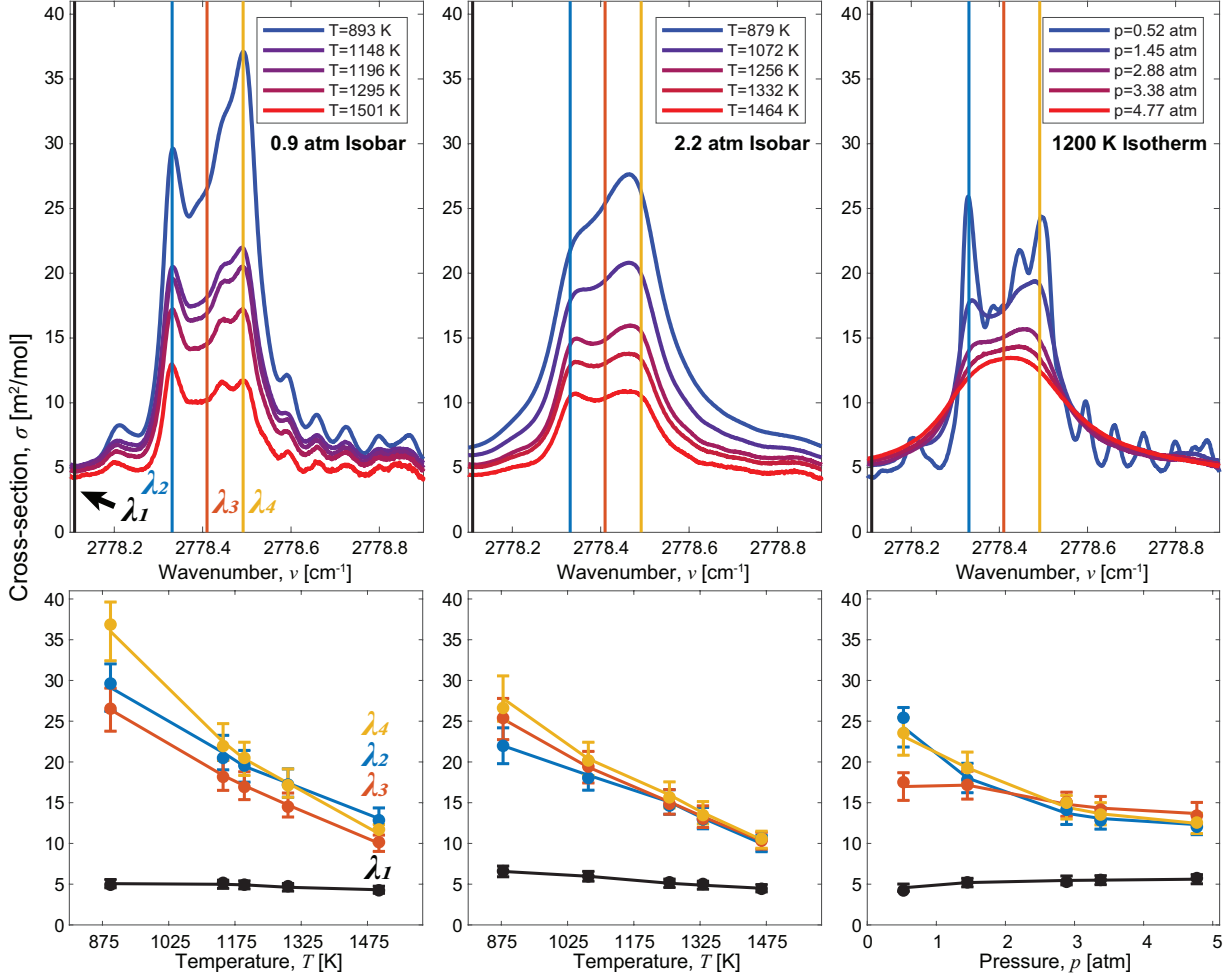


Figure 5: Cross-sections of CH_2O along an isobar at 0.9 atm (Top-left), an isobar at 2.2 atm (Top-middle) and an isotherm at 1200 K (Top-right). The cross-sections given at each temperature and pressure represent an average of the cross-sections collected for a single test. The trends of cross-sections as a function of temperature (Bottom-left and Bottom-middle) and pressure (Bottom-right) at four wavelengths of interest are shown.

wide temperature and pressure range. This insensitivity to pressure and temperature can be attributed to a collection of blended lines with a range of lower-state energies that effectively offset differences in temperature-dependence when aggregated. At higher pressures, the lines under the central feature between $2778.3\text{--}2778.5\text{ cm}^{-1}$ begin to broaden, thus increasing their influence on λ_1 . This results in a slight linear dependence with temperature and pressure that is most pronounced in the 2.2 atm isobar and 1200 K isotherm of Fig. 5.

The wavelengths $\lambda_2\text{--}\lambda_4$ are noted for their proximity near the peak(s) of the absorption cross-section throughout the range of measured temperatures and pressures. Figure 5 shows that, despite the overall spectral absorbance decrease with temperature, λ_2 and λ_4 remain consistently close to the highest cross-section peak values. Given the greater temperature sensitivity of λ_4 compared to that of λ_2 , the ratio of the absorbance at these wavelengths could be used to infer temperature (see Section 4.3). An increase of pressure broadens the lines near λ_2 and λ_4 , smooth-

ing the peaks and valleys of the spectra in the 1200 K isotherm of Fig. 5. The absorption intensity is spread over a wider range of wavenumbers, increasing the cross-section in the wings and decreasing the cross-section between λ_2 and λ_4 . As the cross-sections at λ_2 and λ_4 decrease with pressure, their broadened absorbance is summed near λ_3 , resulting in λ_3 becoming the wavelength with the highest cross-section as the pressure approaches 5 atm.

All cross-section measurements were fit by a multi-parameter linear regression of logarithmic temperature and pressure terms with predictors given in Eq. 5, similar to other works [10]. The integrated absorption cross-section from $2778.1\text{--}2778.8\text{ cm}^{-1}$ was fit using Eq. 6. The coefficients for Eq. 5 are included as supplementary material.

$$\begin{aligned} \sigma(P, T, \nu) = & b_1(\nu) + b_2(\nu) \ln(T) + b_3(\nu) \ln(P) + \\ & b_4(\nu) \ln(T) \ln(P) + b_5(\nu) \ln(T)^2 + \\ & b_6(\nu) \ln(P)^2 + b_7(\nu) \ln(T)^3 + b_8(\nu) \ln(P)^3 \quad (5) \end{aligned}$$

$$A = \int_{2778.1 \text{ cm}^{-1}}^{2778.8 \text{ cm}^{-1}} \sigma(P, T, \nu) d\nu = a_1 + a_2 \ln T + a_3 P \quad (6)$$

Figure 5 shows the spectra's complex dependence on temperature and pressure, requiring the higher order terms of Eq. 5 to sufficiently account for the convoluted effects of line broadening and the reduction of cross-section strength with increasing temperature. The cross-section at each wavenumber is a summation of many lines, each of which have line strengths dependent on temperature and lower-state energy. Each line's contribution to the cross-section at a given wavenumber is dependent on the proximity of its line center to the given wavenumber and the line width (which is a function of the collisional and Doppler broadening). The effects of temperature and pressure in this spectral region are convoluted because as the transition's line widths broaden or narrow, the relative contribution of each individual line to the cross-section at a given wavenumber is impacted. Across the measured spectral range, the integrated cross-sectional area is expected to decrease as temperature increases due to the spread of internal energy across additional modes or states not captured in the target spectral domain, decreasing the state populations for these particular lines of interest. However, integrating over the available spectral domain reduces the pressure dependence, enabling the more simple fit function shown in Eq. 6. A slight pressure dependence remains because as lines broaden past the bounds of integration of Eq. 6, their contribution to the integrated cross-section is not captured in the integral. If Eq. 6 were to be integrated from $\nu = 0$ to ∞ , there would be no expected pressure dependence.

Fitting Eq. 6 to the measured integrated cross-section areas provides the contour in the bottom plot of Fig. 6. The maximum residual between the contour predicted by fitting Eq. 6 and the measured integrated cross-section areas is 6%. The source of this disagreement is likely from the uncertainty in the initial concentration of 1,3,5-trioxane; this is consistent with the $\sim 5\%$ uncertainty of the trioxane cross-section database found in Appendix A. This small uncertainty in integrated cross-section area is reduced by scaling the measured cross-sections such that their integrated areas lie on the contour predicted by fitting Eq. 6. Reported b coefficients of Eq. 5 account for this area scaling. Example plots of the predicted cross-section at λ_2 and λ_4 , along with the predicted area A , are plotted alongside measurement points in Fig. 6.

An estimate of the uncertainty of the cross-section database interpolation is obtained empirically by testing data against the model. This approach involves removing one temperature and pressure condition from the database to create a reduced database. This reduced database is fit with Eq. 5 to obtain the b coefficients of the reduced database, b_{reduced} . The cross-section of the removed temperature and pressure condition is compared to the cross-section predicted by plugging b_{reduced} into Eq. 5 and the residual across the entire spectra is calculated. This process is performed on points within the interior of the conditions

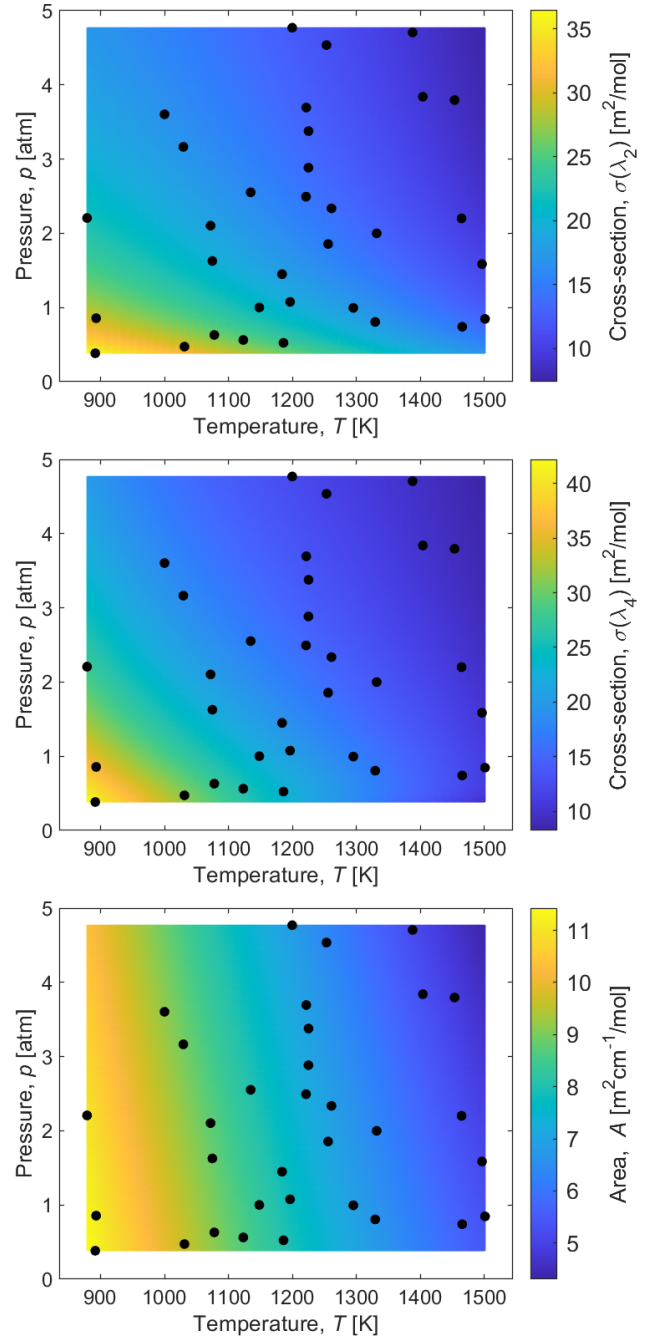


Figure 6: Outputs of Eq. 5 at two wavelengths of interest (Top and Middle) and Eq. 6 (Bottom) plotted against temperature and pressure. Black dots show points where measurements were taken.

map (points not touching a red line in Fig. A.12) and the maximum residual across all interior tests and wavenumbers is 10%. Edge points are not considered since the remaining database must be extrapolated to reconstruct the edge points, biasing the uncertainty upwards. While the maximum residual is 10%, the average residual across all wavenumbers of the interior points is $< 2\%$, reflecting the fact that the majority of conditions have an uncertainty significantly below 10%. This 10%-uncertainty is reflected in the error bars of the bottom three plots of Fig. 5.

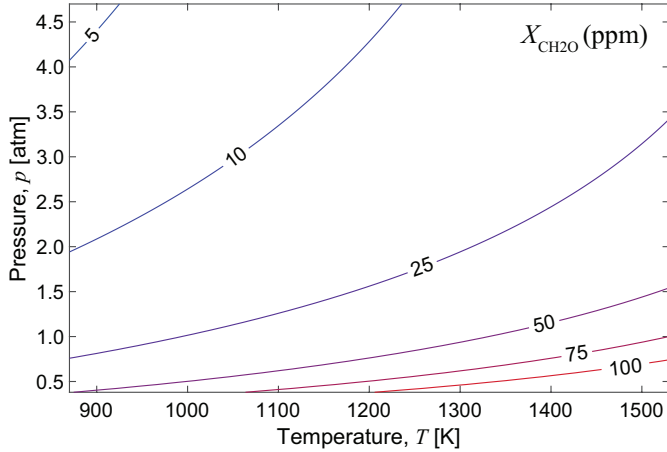


Figure 7: Detection limits of formaldehyde given in parts per million (ppm) for the path length of this study ($L = 10.32$ cm)

Detection limits of formaldehyde are determined by converting the cross-sections to absorbance at each temperature and pressure at the shock tube path length. The noise amplitude of absorbance in the scan is $\Delta\alpha = 0.0025$, by setting a maximum tolerable mole fraction uncertainty of 10%, the limit of detection is found and shown in Fig. 7. Note these detection limits are for a single scan period and do not account for the benefits of averaging.

4.2. Spectral interference

The wavelength region of this study was selected, in part, because of the minimal interference expected from common combustion species. Some simple combustion species, including CO and CO₂, have mature line lists and are predicted to not interfere in this region. More complex molecules, including many common combustion intermediates and some product species, tend to have less reliable predictability with regard to absorption spectra at high temperatures. To verify that the selected wavelength region was indeed largely free of narrow-band interference as predicted, cross-section measurements were taken of common combustion species that could be potential interferers.

Figure 8 shows cross-section measurements of formaldehyde (CH₂O) plotted alongside those of acetaldehyde (CH₃CHO), methane (CH₄), ethylene (C₂H₄) and water (H₂O). Measurements were performed at ~ 1000 K and ~ 1500 K to evaluate both the high and low end of the CH₂O database. Except for H₂O, all species listed above had measurable cross-sections within the spectral region. Fortunately, the spectra of these interfering species were largely flat, representing broadband absorbance that can be subtracted out by fitting the entire spectrum of the formaldehyde cross-sections to adjust the reference baseline magnitude (see next section). Methane was the only species measured that has a distinguishable spectral feature (i.e. differential absorption) in this region, with a peak around 2778.46 cm⁻¹. With regards to this potential interference,

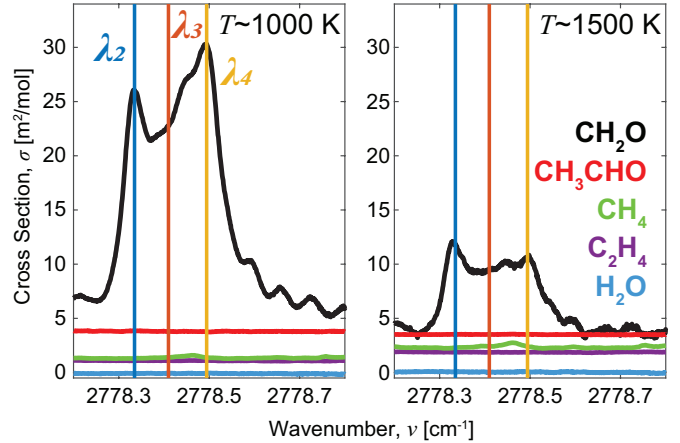


Figure 8: Plot of formaldehyde cross-sections and common combustion interferes at 1000 K (Left) and 1500 K (Right).

the wavelengths λ_1 – λ_4 notably avoid the influence of this methane peak. These spectrally-resolved absorbance measurements for various interfering species can be advantageous in data post-processing for removing absorbance not attributed to CH₂O and identifying species that may be responsible for such baseline absorption.

Spectral interference from common combustion species in the target wavelength domain can be compared to that of Wang et al. [6] at 3.45 μm and Ding et al [8]. at 5.6 μm , both of which also aimed for high-temperature sensing. The magnitude of CH₂O absorption cross-sections reported by Wang et al. at 3.45 μm were approximately 25–40% lower than the values reported in this work (see again Fig. 1). There is minimal interference from H₂O and a comparable interference from both CH₄ and CH₃CHO. Despite being a similar magnitude, the spectral features of the CH₄ spectra at 3.45 μm have a maximum peak to valley cross-section of approximately 1.5 m²/mol whereas the maximum peak to valley cross-section of the CH₄ spectra at 3.6 μm is 0.6 m²/mol (i.e. the CH₄ spectra at 3.6 μm is flatter). The work by Ding et al. reports cross-sections of approximately the same magnitude as this work. There is minimal interference from both H₂O and CH₄ within the spectral region utilized by Ding et al; the CH₃CHO interference is comparable to that reported in this work. Notably, both prior works leverage fixed wavelength laser absorption spectroscopy. This contrasts the spectrally-resolved approach employed here, which has numerous advantages as detailed in the following section.

4.3. Multi-parameter interference-immune sensing

In some combustion environments relevant to formaldehyde sensing, the temperature and/or pressure is unknown—both of which are prerequisites to accurately utilizing cross-sections. While unknown parameters could be left to approximation or independent measurement, here we show that the thermodynamic sensitivity of the spectrally-resolved measurement can be exploited to infer temperature and

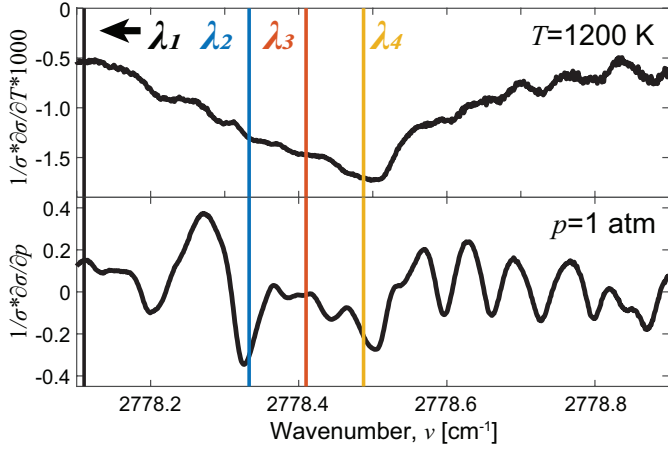


Figure 9: Sensitivity with respect to temperature (Top) and pressure (Bottom) at a temperature of 1200 K and a pressure of 1 atm.

pressure. Notably, this method relies solely on the shape or structure of the spectra, regardless of magnitude, meaning that both temperature and pressure could be extracted with no knowledge of path length or mole fraction.

Temperature and pressure can be inferred from the absorption cross-section by accounting for the spectrally-resolved sensitivity to pressure and temperature, as described here. Equation 7 gives the Taylor expansion of the cross-section about some guessed temperature and pressure (T_0 and p_0). The cross-section at this guessed point is given by σ_0 when T_0 and p_0 are input to Eq. 5.

$$\sigma(T, p) - \sigma_0 = \frac{\partial\sigma_0}{\partial T}(T - T_0) + \frac{\partial\sigma_0}{\partial p}(p - p_0) + \text{H.O.T.} \quad (7)$$

Equation 7 states that taking the difference between a measured cross-section, σ , and a cross-section generated at some guessed temperature and pressure, σ_0 , yields a disagreement approximately proportional to both the spectra's first derivative with respect to temperature and pressure and the difference between the guessed (T_0, p_0) and true (T, p) temperature and pressure of the two spectra. For example, if we measured the 893 K condition shown in the top left of Fig. 5 and estimated the temperature to be 1295 K, the difference between the measured spectra and the estimated spectra generated from the cross-sectional database would be high at λ_2 - λ_4 but relatively low near the edge of the region at λ_1 . The larger disagreement between λ_2 - λ_4 reflects the much steeper derivative of cross-section area with respect to temperature in this spectral region, as seen in the top subplot of Fig. 9. Logically, decreasing the overestimated temperature towards the true value would decrease the disagreement across the entire wavenumber range. Thus, as subsequent guesses converge, the residual between the measured and guessed cross-section will monotonically decrease.

To generalize Eq. 7 to measured absorbance, rather than absorption cross-section, we can use the relation in Eq. 8, where the integrated cross-section and absorbance areas A_σ and A_α are given by $A_\sigma = \int_{\nu_1}^{\nu_2} \sigma(\nu) d\nu$ and $A_\alpha = \int_{\nu_1}^{\nu_2} \alpha(\nu) d\nu$.

$$\frac{\sigma(\nu)}{A_\sigma} = \frac{\alpha(\nu)}{A_\alpha} \quad (8)$$

Normalizing both sides of Eq. 7 by $\sigma_0 \cdot A_\sigma$ and substituting in the relation from Eq. 8 results in Eq. 9. The integrated cross-section area, A_σ , is approximated as $A_\sigma \approx \int_{\nu_1}^{\nu_2} \sigma_0(\nu) d\nu$ since $\sigma(T, p)$ is unknown. This approximation becomes increasingly accurate as the estimated temperature and pressure approach the true values. From Eq. 9, we define the sensitivity of the cross-sections with respect to temperature and pressure as $\frac{1}{\sigma_0} \frac{\partial\sigma_0}{\partial T}$ and $\frac{1}{\sigma_0} \frac{\partial\sigma_0}{\partial p}$ respectively—sample sensitivities are plotted in Fig. 9. Dividing the sensitivities by A_σ provides the normalized sensitivities $\frac{1}{A_\sigma \sigma_0} \frac{\partial\sigma_0}{\partial T}$ and $\frac{1}{A_\sigma \sigma_0} \frac{\partial\sigma_0}{\partial p}$.

$$\frac{\alpha}{A_\alpha \sigma_0} - \frac{1}{A_\sigma} = \frac{1}{A_\sigma \sigma_0} \frac{\partial\sigma_0}{\partial T}(T - T_0) + \frac{1}{A_\sigma \sigma_0} \frac{\partial\sigma_0}{\partial p}(p - p_0) + \text{H.O.T.} \quad (9)$$

Equation 9 can then be used to iteratively solve for temperature and pressure as follows:

1. Make an initial guess for T_0 and p_0 .
2. Calculate σ_0 , A_σ , $\frac{\partial\sigma_0}{\partial T}$ and $\frac{\partial\sigma_0}{\partial p}$ based on the initial guess.
3. Determine the slope, m_T , of the best fit line of $\frac{\alpha}{A_\alpha \sigma_0} - \frac{1}{A_\sigma}$ plotted against $\frac{1}{A_\sigma \sigma_0} \frac{\partial\sigma_0}{\partial T}$.
4. Determine the slope, m_p , of the best fit line of $\frac{\alpha}{A_\alpha \sigma_0} - \frac{1}{A_\sigma}$ plotted against $\frac{1}{A_\sigma \sigma_0} \frac{\partial\sigma_0}{\partial p}$ (example plots are shown in the left column of Fig. 10).
5. Solve for temperature and pressure using the fact that $T = T_0 + m_T$ and $p = p_0 + m_p$.
6. Plug in the solution as the updated guess at step 2 and repeat until values converge; the best fit lines in the left column of Fig. 10 show the slope of the line is zero when the values have converged.

Temperature could also be inferred by simply considering the ratio of absorbance of two select wavelengths within the spectral domain, similar to relatively well-established two-color thermometry methods [25]. However, the resulting uncertainty and noise of the two-color method (for any combination of two specific wavelengths in this region) was found to be higher than fitting the entire spectrum. Utilizing the entire spectral domain, with varying temperature dependence throughout, is analogous to utilizing a multitude of line intensities with varying lower state energy in a multi-line Boltzmann regression to achieve a higher effective sensitivity (or lower uncertainty) over a wider range of conditions [26]. Similarly, previous works have utilized

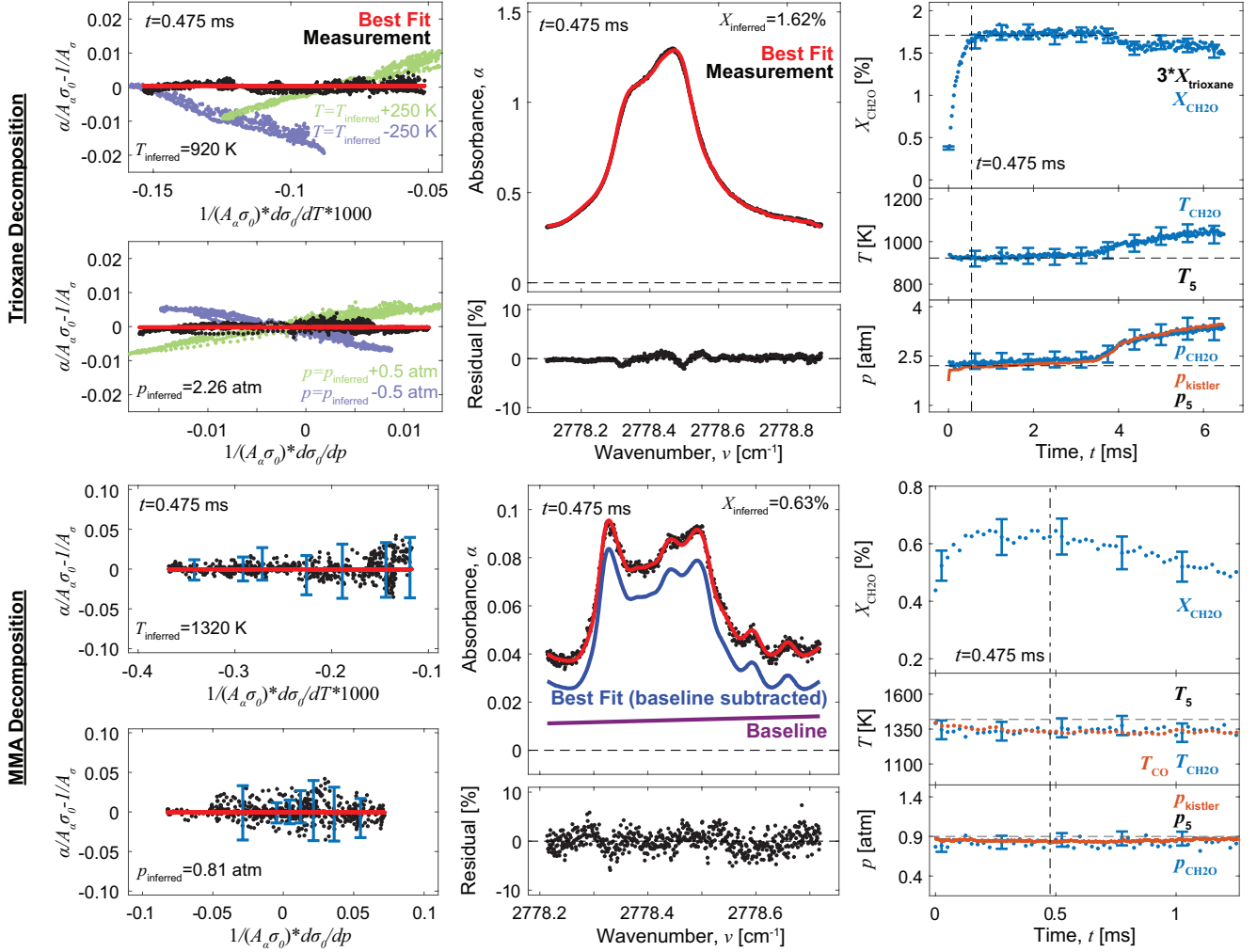


Figure 10: Measurements of the decomposition of 0.57% 1,3,5-trioxane in Ar (Top half) and 3% methyl methacrylate in Ar (Bottom half) after the passage of a reflected shock. (Left) Normalized residual between the guessed cross-section and the measured absorbance plotted against the normalized first derivative of the cross-section with respect to temperature or pressure. A linear fit of the plotted points is shown in red. (Middle) Reconstructed absorbance of a single scan using the cross-section database at the temperature and pressure inferred from the plots in the left column. (Right) Inferred CH_2O mole fraction, temperature, and pressure for the entire test compared to known values where available.

the collision width of individual transitions to infer pressure [27]. The present method extends this approach to spectra with many blended lines that cannot be easily deconvoluted for traditional line fitting and associated analysis.

The multi-parameter spectral fitting procedure was applied as described above to a high SNR trioxane decomposition test in the top half of Fig. 10. To exhibit the range of the method, a methyl methacrylate (MMA) decomposition test is shown in the bottom half of Fig. 10 with a much lower concentration of CH_2O than 1,3,5-trioxane decomposition and thus serving as an independent and lower SNR case. In the MMA experiments, two additional effects are present that can be addressed in post-processing. First, the non-zero baseline resulted in both artificially high and low absorbance values, leading to non-physical values of temperature and pressure. Second, the lower signal-to-

noise ratio caused several outliers in the plot of $\frac{\alpha}{A_\sigma \sigma_0} - \frac{1}{A_\sigma}$ vs. $\frac{1}{A_\sigma \sigma_0} \frac{\partial \sigma_0}{\partial T}$ and $\frac{1}{A_\sigma \sigma_0} \frac{\partial \sigma_0}{\partial p}$ which can bias the slope of the line (m_T, m_p) when weighted equally with other points. To mitigate the erroneous influence of non-zero baselines and low SNR when fitting the CH_2O absorbance, some additional post-processing steps must be included.

Accounting for a non-zero baseline requires the absorbance in Eq. 9 to be modified to include a baseline term, α_{baseline} , such that $\alpha = \alpha_{\text{measured}} + \alpha_{\text{baseline}}$. We use a linear approximation to represent the non-zero baseline, given by $\alpha_{\text{baseline}} = a \cdot \nu + b$. The procedure defined by steps 1–6 can then be performed inside of a least-squares minimization function in which the slope, a , and intercept, b , of the linear baseline are floated. An initial guess of the baseline can be formulated by noting the cross-section of the left wing (λ_1) is approximately $5 \text{ m}^2/\text{mol}$ across the temperature and pressure range i.e.

$\alpha_{\text{baseline}} = 5 \frac{A_\alpha}{A_\sigma} - \alpha_{\text{measured}}(\lambda_1)$. An example of a fitted baseline and the resulting baseline-subtracted spectra from an MMA decomposition experiment can be found in the center bottom row subplot of Fig. 10. As noted in Section 4.2, the spectral interference from most species is invariant over the target spectral domain, justifying the use of a linear baseline. Experiments with elevated CH_4 concentrations may require additional processing steps due to the narrow-band interference of CH_4 between $\lambda_3 - \lambda_4$. The influence of the narrow-band interference between $\lambda_3 - \lambda_4$ can be minimized by excluding the region from the fit or by simultaneously fitting the CH_4 concentration.

Low SNR absorbance tests result in data points with higher uncertainty and potentially skewed results. This poses an issue when performing linear fits on the plots of $\frac{\alpha}{A_\alpha \sigma_0} - \frac{1}{A_\sigma}$ vs. the normalized sensitivities of temperature and pressure as these outlier points can bias the slope of the line. The wings of the spectra have the lowest absorbance, and thus SNR, leading to the highest uncertainty points across the spectral range. The plot of $\frac{\alpha}{A_\alpha \sigma_0} - \frac{1}{A_\sigma}$ vs. $\frac{1}{A_\sigma \sigma_0} \frac{\partial \sigma_0}{\partial T}$ shows that points of higher uncertainty are generally less sensitive (normalized sensitivity values closer to 0). This follows from Fig. 9 where we see that the wings of the spectra have the lowest sensitivity. Unlike with temperature, Fig. 9 shows that the points most sensitive to pressure are more evenly distributed throughout the spectral range resulting in the uncertainty, as represented by error bar magnitude, being more evenly distributed throughout the points of the plot of $\frac{\alpha}{A_\alpha \sigma_0} - \frac{1}{A_\sigma}$ vs. $\frac{1}{A_\sigma \sigma_0} \frac{\partial \sigma_0}{\partial p}$. Therefore, we fit the data using a least-squares algorithm adjusted with error bars [28], which provided a more accurate temperature and pressure measurement from low SNR signals. The error bars of the leftmost plots of Fig. 10 are the combined effects of the uncertainty due to noise in the absorbance signal and the uncertainty due to truncating the higher order terms (H.O.T.) of Eq. 9 added together in quadrature. A conservative value of absorbance noise in this experiment is $\Delta\alpha = 0.0025$ and the higher order terms are approximated with Eq. 10. At high signal-to-noise ratios (top half of Fig.10), the higher order terms dominate the error bars; however, at low signal-to-noise ratios (bottom half of Fig.10), the absorbance noise dominates.

$$\begin{aligned} \text{H.O.T} \approx & \frac{1}{2A_\sigma \sigma_0} \frac{\partial^2 \sigma_0}{\partial T^2} (T - T_0)^2 + \\ & \frac{1}{2A_\sigma \sigma_0} \frac{\partial^2 \sigma_0}{\partial p^2} (p - p_0)^2 + \\ & \frac{1}{A_\sigma \sigma_0} \frac{\partial^2 \sigma_0}{\partial p \partial T} (T - T_0)(p - p_0) \quad (10) \end{aligned}$$

These error bars represent the relative weighting of those individual points in the least-squares algorithm and are not meant to capture the spread of nearby data points. It should be noted that this approach can be similarly employed to effectively exclude or minimize certain regions

of the spectra that may include differential absorption of an interferer, such as the aforementioned methane line.

The right column of Fig. 10 shows time-resolved measurements of CH_2O mole fraction, temperature, and pressure for trioxane decomposition and MMA decomposition experiments. In the trioxane test, the mole fraction of CH_2O rapidly rises from zero as the trioxane dissociates before plateauing at the expected amount – three times the initial mole fraction of trioxane. As the initial concentration of trioxane is low (0.57%), only a small temperature drop occurs beyond the post-reflected shock temperature. The pressure inferred from the CH_2O spectra was relatively consistent with the pressure transducer (Kistler) measurement throughout the test. After 3.75 ms, the reflected shock interacts with the contact surface creating an increase in pressure, which is seen in both the spectrally inferred pressure and the pressure transducer measurement. This pressure increase coincides with a temperature increase, which leads to further CH_2O dissociation as can be seen in the respective plot above. In the MMA decomposition test, we observe rapid dissociation of the MMA near 1350 K. At the first measurement point, the mole fraction of CH_2O has already reached 0.4%. During the MMA dissociation, here observed from the rise in CH_2O mole fraction, the temperature drops more significantly from the post-reflected shock temperature than seen in the trioxane test; this is expected as the initial MMA concentration (3%) is much higher than that of trioxane (0.57%) in the respective tests. After the initial decomposition period and associated temperature drop, the temperature remains relatively constant. The temperature inferred from CH_2O shows good agreement with CO thermometry data obtained with the method utilized by Sanders et al. applied to MMA decomposition [24]. As with the trioxane test, we observe good agreement between the measured pressure transducer and CH_2O spectrally inferred pressures, as both remain nearly constant throughout the test time. It should be noted that the time-histories of pressure and temperature inferred from the CH_2O spectra were used to calculate the CH_2O mole fraction. The results of these tests demonstrate that pressure, temperature, and CH_2O mole fraction can all be simultaneously measured using the absorption cross-section database developed in this work.

As demonstrated, spectrally-resolved data attained at time-scales relevant to combustion offer significant advantages in CH_2O sensing. Previous studies targeting CH_2O absorption have generally employed fixed-wavelength measurements and cross-section correlations at two or three wavelengths to recover species concentration at high measurement rates. In such works, the time-dependent experiment of interest is repeated for each time-resolved absorption measurement at “online” and “offline” wavelengths. This strategy has been readily employed for multiple reasons, including to avoid complex detailed modeling of the high-temperature broadband CH_2O spectra and to account for potential broadband interference from other combustion species. In any case, the fixed-wavelength online/offline

approach requires running multiple experiments at each desired condition, thus relying on a high level of test repeatability and independent measurements of cross-section scaling parameters (such as pressure and temperature) to accurately recover molecular abundance. As such, this well-established approach generally precludes application for true real-time sensing of CH_2O in dynamic environments without multiplexing multiple light sources. In contrast, the work presented here details a spectrally-resolved sensing method that leverages knowledge of pressure- and temperature-dependent spectral structure to enable robust, interference-immune, and time-resolved sensing of formaldehyde in environments with transient gas properties.

5. Conclusion

Absorption cross-sections of CH_2O were measured near $3.6 \mu\text{m}$, a spectral domain of strong absorptivity associated with the overlapping $^{\text{Q}}\text{Q}_5$ branch of the ν_1 band and the $^{\text{P}}\text{Q}_7$ branch of the $\nu_2+\nu_4$ combination band. Formaldehyde cross-sections were attained over a range of combustion-relevant pressures (0.4–4.8 atm) and temperatures (900–1500 K). This spectral region is favorable for sensing applications due to minimal interference from other relevant combustion species and high absorption intensity that enables detection limits in the tens of ppm (at ~ 10 cm path length) over a wide range of conditions. While the cross-section magnitudes near $3.6 \mu\text{m}$ are comparable to other infrared peaks used for high-temperature sensing, the rapid-tuning (40 kHz) and spectrally-resolved sensing approach combined with the strong local spectral dependence on temperature and pressure enable more robust and efficient data collection and processing relative to fixed-wavelength methods previously used for formaldehyde chemical kinetics studies. A novel spectral fitting method is introduced to infer the temperature and pressure from the normalized spectra, whereafter mole fraction can be quantitatively determined without independent measurements or estimates of these properties and baseline interference can be rejected. In aggregate, this work provides a novel data set of high-temperature CH_2O absorption cross-sections that may serve as modeling targets in an important infrared region and presents a new approach for multi-parameter sensing from localized cross-sections with complex temperature and pressure dependence.

Acknowledgements

This work was supported by the U.S. National Science Foundation, CAREER Award No. 1752516, and by the Air Force Office of Scientific Research (AFOSR) Young Investigator Program (YIP) award no. FA9550-19-1-0062 with Dr. Chiping Li as Program Officer. ICS acknowledges support from The Natural Sciences and Engineering Research Council of Canada.

Appendix A. Trioxane cross-sectional database

Measured absorption cross-sections of 1,3,5-trioxane are shown in Fig. A.11. The spectra at low pressures (between 11 and 65 Torr) contain many peaks and valleys that exhibit strong sensitivity to pressure. Around the largest peak (2778.62 cm^{-1}), the pressure sensitivity is around $-0.11 \text{ m}^2 \cdot \text{mol}^{-1}/\text{Torr}$. Above 65 Torr, only one to two stronger peaks are present and the spectral dependence on pressure is significantly lessened. The sensitivity at 2778.62 cm^{-1} is $-0.007 \text{ m}^2 \cdot \text{mol}^{-1}/\text{Torr}$ in the 65–246 Torr range. Preliminary measurements helped to identify the pressure sensitivity of the spectra which informed the targeted pressure spacing for subsequent tests.

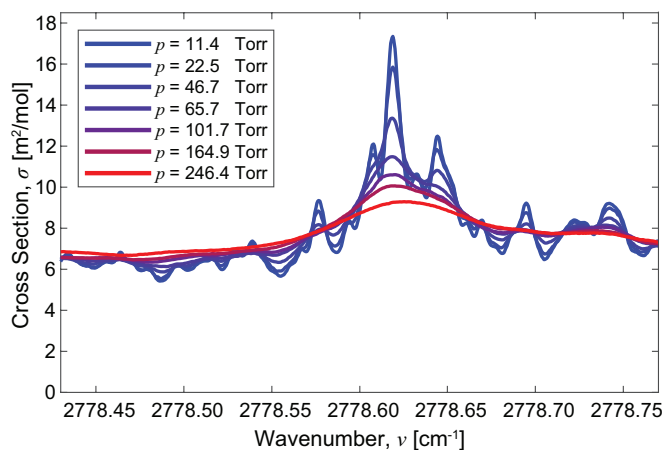


Figure A.11: Sample cross-sections of 0.5% 1,3,5-trioxane in 99.5% argon

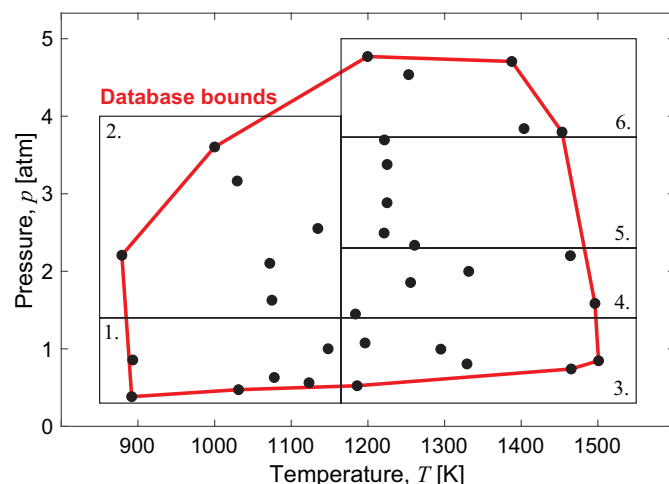


Figure A.12: Plot of temperatures and pressure at which database measurements were taken. Black boxes labeled 1–6 bound regions where data is shown in Fig. A.13. The region in which the database can be used without extrapolation is bounded in red.

To ensure the pressure dependency was sufficiently captured, one data point would be removed from the database and the measured spectra would be compared to the predicted spectra produced from interpolating between the

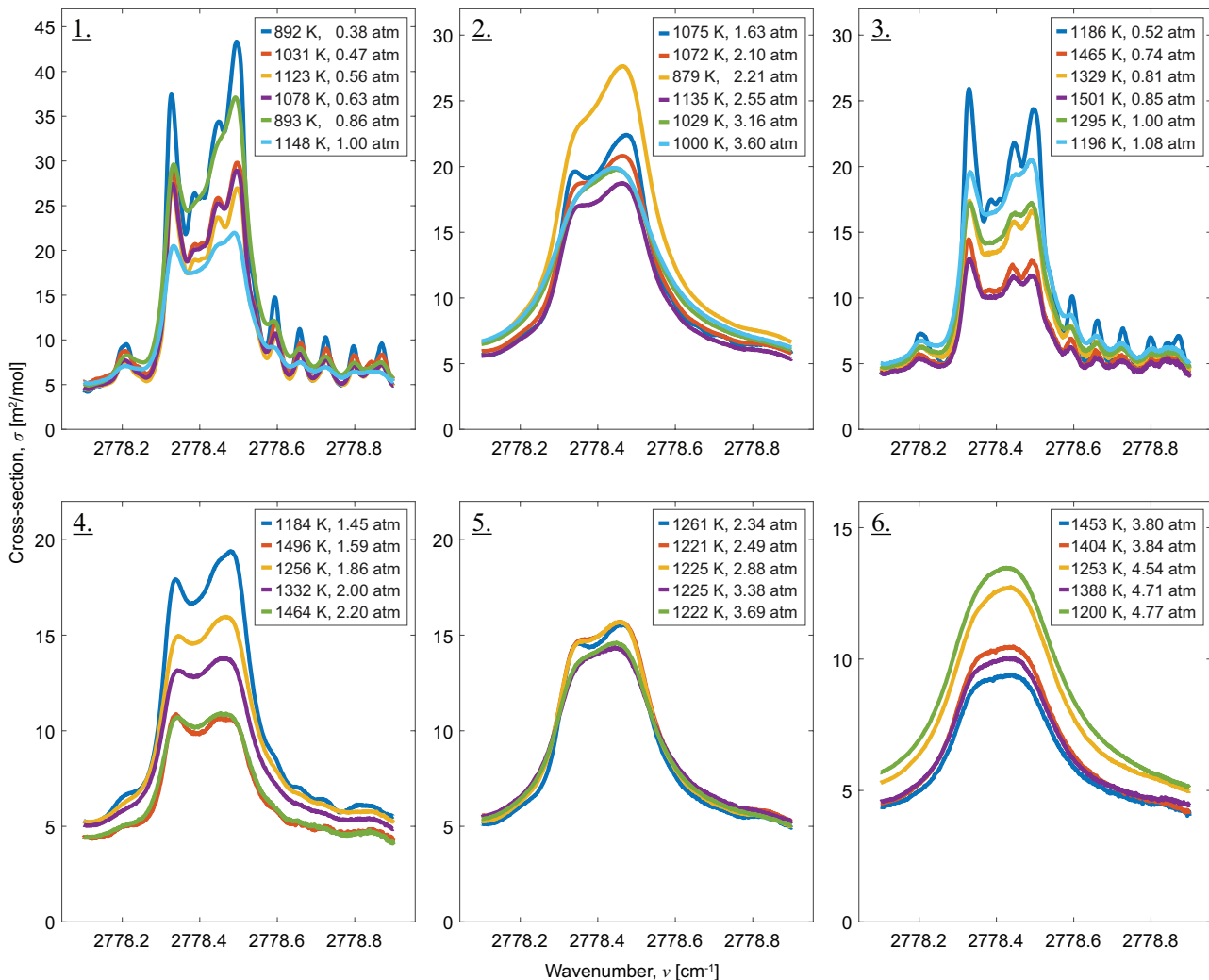


Figure A.13: Plot of all cross-section measurements made in this study. The cross-sections given at each temperature and pressure represent an average of the cross-sections collected for a single test. Tests of similar conditions are grouped as noted in Fig. A.12.

nearest experimental conditions. We then calculated the spectrally-resolved disagreement between the interpolated spectra and measured spectra. When the maximum disagreement across the wavenumber range was $< 5\%$, the pressure spacing was considered adequate for this study. This sets the maximum uncertainty of the trioxane database as $\sim 5\%$. This method was used to provide an upper bound of the uncertainty in the trioxane database—the true uncertainty is likely lower when the removed data point is reinserted in the database. Additionally, taking the maximum of the disagreement across the spectral range overestimates the overall uncertainty since the average of the disagreement was consistently $< 1\%$.

Appendix B. Supplementary Material

The supplementary material of this paper consists of three files: `H2CO_coefficients.csv`, `sig_fun.mat`, and `H2CO_xsec.csv`. `H2CO_coefficients.csv` is a comma-separated values file of the coefficients obtained by fit-

ting Eq. 5 to the measured cross-sections. The first column is the wavenumber and the subsequent 8 columns are the coefficients b_1 – b_8 . `sig_fun.mat` is Eq. 5 and takes `H2CO_coefficients.csv` as an input along with temperature and pressure to reconstruct the cross-section at that point. It is important to note that `sig_fun.mat` can take any temperature and pressure as an input but caution should be exercised when using the database around or outside the red outline in Fig. A.12, past which the data will be extrapolated. `H2CO_xsec.csv` is a comma-separated values file containing the measured cross-sections as a function of wavenumber and their corresponding temperature and pressure. Figure A.13 shows a plot of all measurements made. For readability, tests of similar conditions are grouped together into the regions labeled 1–6 in Fig. A.12.

References

- [1] G. Zasowski, F. Kemper, D. M. Watson, E. Furlan, C. Bohac, C. Hull, J. D. Green, *Spitzer Infrared Spectrograph Observations of Class I/II Objects in Taurus: Composition and Thermal History of the Circumstellar Ices*, *The Astrophysical Journal* 694 (1) (2009) 459–478. doi:10.1088/0004-637X/694/1/459. URL <https://iopscience.iop.org/article/10.1088/0004-637X/694/1/459>
- [2] S. N. Milam, A. J. Remijan, M. Womack, L. Abrell, L. M. Ziurys, S. Wyckoff, A. J. Apponi, D. N. Friedel, L. E. Snyder, J. M. Veal, P. Palmer, L. M. Woodney, M. F. A'Hearn, J. R. Forster, M. C. H. Wright, I. de Pater, S. Choi, M. Gesmundo, *Formaldehyde in Comets C/1995 O1 (Hale-Bopp), C/2002 T7 (LINEAR), and C/2001 Q4 (NEAT): Investigating the Cometary Origin of H₂CO*, *The Astrophysical Journal* 649 (2) (2006) 1169–1177. doi:10.1086/506501. URL <https://iopscience.iop.org/article/10.1086/506501>
- [3] R. D. Reitz, *Directions in internal combustion engine research*, *Combustion and Flame* 160 (1) (2013) 1–8, publisher: The Combustion Institute. ISBN: 0010-2180. doi:10.1016/j.combustflame.2012.11.002. URL <http://dx.doi.org/10.1016/j.combustflame.2012.11.002>
- [4] Y. Tao, G. P. Smith, H. Wang, *Critical kinetic uncertainties in modeling hydrogen / carbon monoxide , methane , methanol , formaldehyde , and ethylene combustion*, *Combustion and Flame* 195 (2018) 18–29, publisher: Elsevier Inc. doi:10.1016/j.combustflame.2018.02.006. URL <https://doi.org/10.1016/j.combustflame.2018.02.006>
- [5] G. Herzberg, *Molecular Spectra and Molecular Structure II. Infrared and Raman Spectra of Polyatomic Molecules*, D. Van Nostrand Company, Inc., Princeton, NJ, 1945.
- [6] S. Wang, D. F. Davidson, R. K. Hanson, *High-temperature laser absorption diagnostics for CH₂O and CH₃CHO and their application to shock tube kinetic studies*, *Combustion and Flame* 160 (10) (2013) 1930–1938, publisher: The Combustion Institute. doi:10.1016/j.combustflame.2013.05.004. URL <http://dx.doi.org/10.1016/j.combustflame.2013.05.004>
- [7] K. Tanaka, S. Sugano, H. Nagata, S. Sakaida, M. Konno, *Quantitative measurements of formaldehyde in the low-temperature oxidation of iso-octane using mid-infrared absorption spectroscopy*, *Applied Physics B: Lasers and Optics* 125 (10) (2019) 1–9, publisher: Springer Berlin Heidelberg ISBN: 0123456789. doi:10.1007/s00340-019-7304-y. URL <https://doi.org/10.1007/s00340-019-7304-y>
- [8] Y. Ding, S. Wang, R. K. Hanson, *Sensitive and interference-immune formaldehyde diagnostic for high-temperature reacting gases using two-color laser absorption near 5.6 μm*, *Combustion and Flame* 213 (2020) 194–201, publisher: Elsevier Inc. doi:10.1016/j.combustflame.2019.11.042. URL <https://doi.org/10.1016/j.combustflame.2019.11.042>
- [9] Y. Ding, W. Peng, C. Strand, R. Hanson, *Quantitative measurements of broad-band mid-infrared absorption spectra of formaldehyde, acetaldehyde, and acetone at combustion-relevant temperatures near 5.7 μm*, *Journal of Quantitative Spectroscopy and Radiative Transfer* 248 (2020) 106981, publisher: JQSRT. doi:10.1016/j.jqsrt.2020.106981. URL <https://linkinghub.elsevier.com/retrieve/pii/S0022407319308842>
- [10] P. Biswas, R. Choudhary, A. Panda, D. F. Davidson, R. K. Hanson, *A mid-IR laser absorption diagnostic for measuring formaldehyde at high pressures and its demonstration in shock tubes*, *Combustion and Flame* 245 (2022) 112366. doi:10.1016/J.COMBUSTFLAME.2022.112366. URL <https://linkinghub.elsevier.com/retrieve/pii/S0010218022003819>
- [11] I. Gordon, L. Rothman, R. Hargreaves, R. Hashemi, E. Karlovets, F. Skinner, E. Conway, C. Hill, R. Kochanov, Y. Tan, P. Wcislo, A. Finenko, K. Nelson, P. Bernath, M. Birk, V. Boudon, A. Campargue, K. Chance, A. Coustenis, B. Drouin, J. Flaud, R. Gamache, J. Hodges, D. Jacquemart, E. Mlawer, A. Nikitin, V. Perevalov, M. Rotger, J. Tennyson, G. Toon, H. Tran, V. Tyuterev, E. Adkins, A. Baker, A. Barbe, E. Canè, A. Császár, A. Dudaryonok, O. Egorov, A. Fleisher, H. Fleurbaey, A. Foltynowicz, T. Furtenbacher, J. Harrison, J. Hartmann, V. Horneman, X. Huang, T. Karman, J. Karns, S. Kass, I. Kleiner, V. Kofman, F. Kwabia-Tchana, N. Lavrentieva, T. Lee, D. Long, A. Lukashevskaya, O. Lyulin, V. Makhnev, W. Matt, S. Massie, M. Melosso, S. Mikhailenko, D. Mondelain, H. Müller, O. Naumenko, A. Perrin, O. Polyansky, E. Raddaoui, P. Raston, Z. Reed, M. Rey, C. Richard, R. Tóbiás, I. Sadiek, D. Schwenke, E. Starikova, K. Sung, F. Tamassia, S. Tashkun, J. Vander Auwera, I. Vasilenko, A. Viganin, G. Villanueva, B. Vispoel, G. Wagner, A. Yachmenev, S. Yurchenko, The HITRAN2020 molecular spectroscopic database, *Journal of Quantitative Spectroscopy and Radiative Transfer* 277 (2022) 107949, publisher: Elsevier Ltd. doi:10.1016/j.jqsrt.2021.107949.
- [12] T. Delahaye, R. Armante, N. A. Scott, N. Jacquinet-Husson, A. Chédin, L. Crépeau, C. Crevoisier, V. Douet, A. Perrin, A. Barbe, V. Boudon, A. Campargue, L. H. Coudert, V. Ebert, J. M. Flaud, R. R. Gamache, D. Jacquemart, A. Jolly, F. Kwabia Tchana, A. Kyuberis, G. Li, O. M. Lyulin, L. Manceron, S. Mikhailenko, N. Moazzen-Ahmadi, H. S. Müller, O. V. Naumenko, A. Nikitin, V. I. Perevalov, C. Richard, E. Starikova, S. A. Tashkun, V. G. Tyuterev, J. Vander Auwera, B. Vispoel, A. Yachmenev, S. Yurchenko, The 2020 edition of the GEISA spectroscopic database, *Journal of Molecular Spectroscopy* 380 (July) (2021). doi:10.1016/j.jms.2021.111510.
- [13] A. F. Al-Refaie, A. Yachmenev, J. Tennyson, S. N. Yurchenko, *ExoMol line lists – VIII. A variationally computed line list for hot formaldehyde*, *Monthly Notices of the Royal Astronomical Society* 448 (2) (2015) 1704–1714. doi:10.1093/mnras/stv091. URL <http://academic.oup.com/mnras/article/448/2/1704/1059875/ExoMol-line-lists-VIII-A-variationally-computed>
- [14] A. R. Al-Derzi, J. Tennyson, S. N. Yurchenko, M. Melosso, N. Jiang, C. Puzzarini, L. Dore, T. Furtenbacher, R. Tóbiás, A. G. Császár, *An improved rovibrational linelist of formaldehyde, H₂12C₁₆O*, *Journal of Quantitative Spectroscopy and Radiative Transfer* 266 (2021) 107563, publisher: Elsevier Ltd. doi:10.1016/j.jqsrt.2021.107563. URL <https://doi.org/10.1016/j.jqsrt.2021.107563>
- [15] J. Tennyson, S. N. Yurchenko, A. F. Al-Refaie, V. H. Clark, K. L. Chubb, E. K. Conway, A. Dewan, M. N. Gorman, C. Hill, A. E. Lynas-Gray, T. Mellor, L. K. McKemmish, A. Owens, O. L. Polyansky, M. Semenov, W. Somogyi, G. Tinetti, A. Upadhyay, I. Waldmann, Y. Wang, S. Wright, O. P. Yurchenko, The 2020 release of the ExoMol database: Molecular line lists for exoplanet and other hot atmospheres, *Journal of Quantitative Spectroscopy and Radiative Transfer* 255, arXiv:2007.13022 Publisher: Elsevier Ltd (2020). doi:10.1016/j.jqsrt.2020.107228.
- [16] R. B. Nerf, *Pressure broadening and shift in the millimeter-wave spectrum of formaldehyde*, *Journal of Molecular Spectroscopy* 58 (3) (1975) 451–473. doi:10.1016/0022-2852(75)90225-8.
- [17] F. A. Bendana, D. D. Lee, C. Wei, D. I. Pineda, R. M. Spearrin, *Line mixing and broadening in the v(1→3) first overtone bandhead of carbon monoxide at high temperatures and high pressures*, *Journal of Quantitative Spectroscopy and Radiative Transfer* 239 (2019) 106636, publisher: Elsevier Ltd. doi:10.1016/j.jqsrt.2019.106636. URL <https://linkinghub.elsevier.com/retrieve/pii/S0022407319304042>
- [18] D. D. Lee, F. A. Bendana, A. P. Nair, D. I. Pineda, R. M. Spearrin, *Line mixing and broadening of carbon dioxide by argon in the v₃ bandhead near 4.2 μm at high temperatures and high pressures*, *Journal of Quantitative Spectroscopy and Radiative Transfer* 253 (2020) 107135. doi:10.1016/j.jqsrt.2020.107135.
- [19] J. William Parks McKinnell, *The Sorption of Some Diatomic Gases On Stainless Steel And Iron Surfaces And Its Relation*

- To Passivity (1956).
- [20] O. Mathieu, E. Petersen, [Experimental and modeling study on the high-temperature oxidation of Ammonia and related NOx chemistry](#), *Combustion and Flame* 162 (3) (2015) 554–570, publisher: The Combustion Institute. doi:10.1016/j.combustflame.2014.08.022.
URL <http://dx.doi.org/10.1016/j.combustflame.2014.08.022>
- [21] D. I. Pineda, F. A. Bendana, K. K. Schwarm, R. M. Spearrin, [Multi-isotopologue laser absorption spectroscopy of carbon monoxide for high-temperature chemical kinetic studies of fuel mixtures](#), *Combustion and Flame* 207 (2019) 379–390. doi:10.1016/j.combustflame.2019.05.030.
URL <https://linkinghub.elsevier.com/retrieve/pii/S0010218019302433>
- [22] J. D. Anderson, *Modern Compressible Flow*, McGraw-Hill, 2002.
- [23] M. F. Campbell, S. Wang, C. S. Goldenstein, R. M. Spearrin, A. M. Tulgestke, L. T. Zaczek, D. F. Davidson, R. K. Hanson, [Constrained reaction volume shock tube study of n-heptane oxidation: Ignition delay times and time-histories of multiple species and temperature](#), *Proceedings of the Combustion Institute* 35 (1) (2015) 231–239, publisher: The Combustion Institute ISBN: 1540-7489. doi:10.1016/j.proci.2014.05.001.
URL <http://dx.doi.org/10.1016/j.proci.2014.05.001>
- [24] I. C. Sanders, N. M. Kuenning, N. Q. Minesi, D. I. Pineda, R. M. Spearrin, [Methyl methacrylate thermal decomposition: Modeling and laser spectroscopy of species time-histories behind reflected shock waves](#), *Fuel* 335 (2023) 126846, publisher: Elsevier Ltd. doi:10.1016/j.fuel.2022.126846.
URL <https://doi.org/10.1016/j.fuel.2022.126846>
- [25] R. M. Spearrin, W. Ren, J. B. Jeffries, R. K. Hanson, [Multi-band infrared CO2 absorption sensor for sensitive temperature and species measurements in high-temperature gases](#), *Applied Physics B* 116 (4) (2014) 855–865, ISBN: 0946-2171. doi:10.1007/s00340-014-5772-7.
- [26] N. Q. Minesi, M. O. Richmond, C. C. Jelloian, N. M. Kuenning, A. P. Nair, R. M. Spearrin, [Multi-line Boltzmann regression for near-electronvolt temperature and CO sensing via MHz-rate infrared laser absorption spectroscopy](#), *Applied Physics B: Lasers and Optics* 128 (12) (Dec. 2022). doi:10.1007/s00340-022-07931-7.
URL <https://link.springer.com/10.1007/s00340-022-07931-7>
- [27] A. P. Nair, N. Q. Minesi, N. M. Kuenning, A. R. Keller, R. M. Spearrin, [Optical pressure sensing at MHz rates via collisional line broadening of carbon monoxide: uncertainty quantification in reacting flows](#), *Applied Physics B* 129 (4) (2023) 51. doi:10.1007/s00340-023-07985-1.
URL <https://link.springer.com/10.1007/s00340-023-07985-1>
- [28] D. York, N. M. Evensen, M. L. Martinez, J. De Basabe Delgado, [Unified equations for the slope, intercept, and standard errors of the best straight line](#), *American Journal of Physics* 72 (3) (2004) 367–375, ISBN: 0002-9505. doi:10.1119/1.1632486.
URL <http://aapt.scitation.org/doi/10.1119/1.1632486>